



Time-domain numerical modelling of the connector forces in a modular pontoon floating breakwater under regular and irregular oblique waves

A.J. Cebada-Relea, M. López^{*}, M. Aenlle

DyMAST Research Group and Department of Construction and Manufacturing Engineering, University of Oviedo, Polytechnic School of Mieres, C/ Gonzalo Gutiérrez Quirós s/n 33600, Mieres, Asturias, Spain

ARTICLE INFO

Keywords:

Floating structures
Fluid-structure interaction
Model validation
Potential flow theory
Aqwa

ABSTRACT

Floating breakwaters are an interesting alternative to bottom-fixed structures due to their lower cost and environmental impact. Nonetheless, structural failures in the module connections are frequent. Accurate analysis of the hydrodynamic response is therefore crucial to their structural design. This article reports on numerical modelling of the forces on the module connectors in a modular pontoon breakwater. The study case was an array of five pontoons with elastic mooring lines under regular and irregular oblique waves. A 3D Boundary Element Method (BEM) solver was applied to find the velocity potentials and to characterize the frequency-domain response. The time-domain response of the floating breakwater is calculated along with the forces in the elastic mooring lines and module joints. Nonlinear hydrodynamic effects were reproduced by calculating the Froude-Krylov and hydrostatic forces over the instantaneous wetted surface at each time step. The response of the modular array under regular waves was then compared with previous experiments. After calibrating connector stiffness, the numerical and experimental results were in good agreement. Finally, the floating structure's response to regular and irregular waves was compared. The results revealed that simulation of only regular waves underestimates maximum connection forces by one order of magnitude.

1. Introduction

Breakwaters attenuate waves in harbour areas providing safe harbourage and minimizing port operation downtimes (Lopez et al., 2015). The foundations of these massive constructions are commonly laid on the seabed at the expense of high environmental impact. Alternatively, several typologies of floating breakwaters have been proposed as a low-cost and environmentally-friendly solution (McCartney, 1985). Among the different configurations of floating breakwaters, the most common types are the box, pontoon, Y-frame, mat, tethered and horizontal plates (Fig. 1). This study focused on pontoon floating breakwaters, which consist of several concrete modules moored to the seabed and connected to each other by flexible connectors.

An example of this typology is the modular floating breakwater in the Port of Figueras in the Eo River estuary in northern Spain (Fig. 2). The local port authorities have reported frequent structural failures in this breakwater after extreme wind waves, starting with the module connectors breaking. This causes the unrestrained modules to undergo very strong relative movement, resulting in collisions between adjacent modules and reduction in the wave dissipation efficiency of the

breakwater. It may be inferred from this observation that the pontoon design installed at the Port of Figueras is unable to withstand the local wave conditions due to excessive module connector forces (Cebada and López, 2020).

Similar structural damage, in which the connections appear to be the Achilles's heel in their design, has been reported in other floating breakwaters worldwide (Martinelli et al., 2008). Analysis of the module connector forces is therefore of paramount importance for an integrated and sustainable design. The floating breakwater response and internal forces in the connectors can be studied with physical and/or numerical models.

The hydrodynamic response of these structures, and particularly, their wave transmission coefficients (e.g. Cheng et al., 2020; Dong et al., 2008; Ruol et al., 2013), are commonly tested with physical models in wave tanks. However, research on the structural response of floating breakwaters is scarce. Apart from wave transmission, Martinelli et al. (2008) studied the loads in moorings and connectors of different floating breakwater layouts. Peña et al. (2011) carried out physical model tests on a pontoon similar to that of the Port of Figueras under regular waves, and analysed the mechanical loads on the mooring lines and the module

^{*} Corresponding author.

E-mail address: mario.lopez@uniovi.es (M. López).

<https://doi.org/10.1016/j.oceaneng.2021.110263>

Received 23 July 2021; Received in revised form 22 October 2021; Accepted 26 November 2021

Available online 18 December 2021

0029-8018/© 2021 The Authors.

Published by Elsevier Ltd.

This is an open access article under the CC BY-NC-ND license

(<http://creativecommons.org/licenses/by-nc-nd/4.0/>).

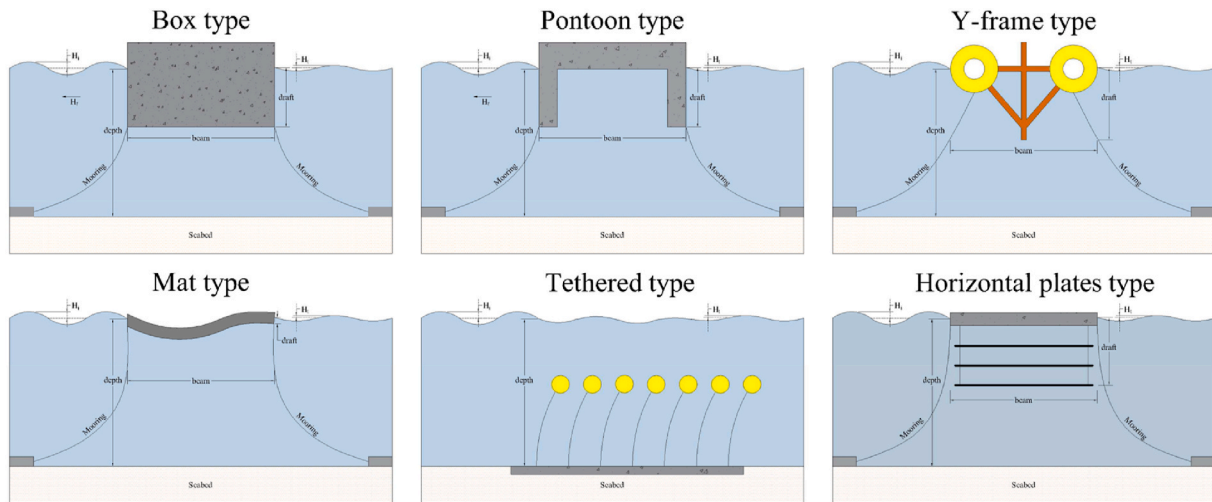


Fig. 1. Main types of floating breakwaters.



Fig. 2. Floating breakwater at the Port of Figueras (Spain): location (left) and pictures of the structure after connector breakage (right).

connectors. Ferreras et al. (2014) also studied the effect of the mooring typology and the module layout on the structural behaviour of modular pontoons under regular waves, and applied the results to the design of a breakwater similar to the one at the Port of Figueras. More recently, image processing algorithms have been applied to study the hydroelastic and structural responses of a modular pontoon under the action of perpendicular and oblique regular waves (Loukogeorgaki et al., 2017). The structural response of other types of floating breakwater, such as the box subtype, have also been studied experimentally (Loukogeorgaki et al., 2014).

Several different approaches to numerical modelling analysis have been applied to wave-structure interaction of floating breakwaters during the last few decades. 2D modelling is the most widely used methodology, but it cannot reproduce the wave obliquity responsible for severe loads on module connections (Martinelli et al., 2008). Traditional 2D linear methods include the finite element method (FEM) (Elchahal et al., 2009; Sannasiraj et al., 2001), the element-free Galerkin method (Lee and Cho, 2003), and the boundary element method (BEM) (Williams et al., 2000). Other novel techniques applied to pontoon-type floating breakwaters are the Navier-Stokes solvers, which include two well-differentiated groups: the finite volume method, based on structured Eulerian meshes, and the volume of fluid technique for tracking the liquid-gas interface (Ji et al., 2018), and smoothed-particle

hydrodynamics based on Lagrangian mesh-free methods (Liu and Wang, 2020). Both solvers include nonlinear hydrodynamic effects in the wave-structure interaction solution, but at a high computational cost.

3D models based on potential flow theory have therefore been proposed to evaluate complex layouts with mooring lines and connection elements. Abul-Azm and Gesraha (2000) studied the hydrodynamic properties of a long rigid pontoon floating in oblique waves with only three rigid-body degrees of freedom (DoF) in the frequency domain. 3D hydrodynamic linear models have been used to assess the performance of hinged floating breakwaters under the action of normal regular waves (Loukogeorgaki and Angelides, 2005), as well as for several different wave headings (e.g. Diamantoulaki and Angelides, 2010; Teng et al., 2014). Cable-moored hinged floating breakwaters were analysed by coupling the hydrodynamic formulation of the floating body with static and dynamic analysis of the mooring lines (Diamantoulaki and Angelides, 2011). This approach was applied to the performance of a pontoon-type floating structure under the effects of regular waves with particular focus on mooring line tension and the hydroelastic structural response (Loukogeorgaki et al., 2015). A similar approach was applied to solve the forces on the connectors in an array of box-type floating breakwaters under irregular waves (Ćatipović et al., 2019).

In addition to these frequency-domain models, time-domain solvers

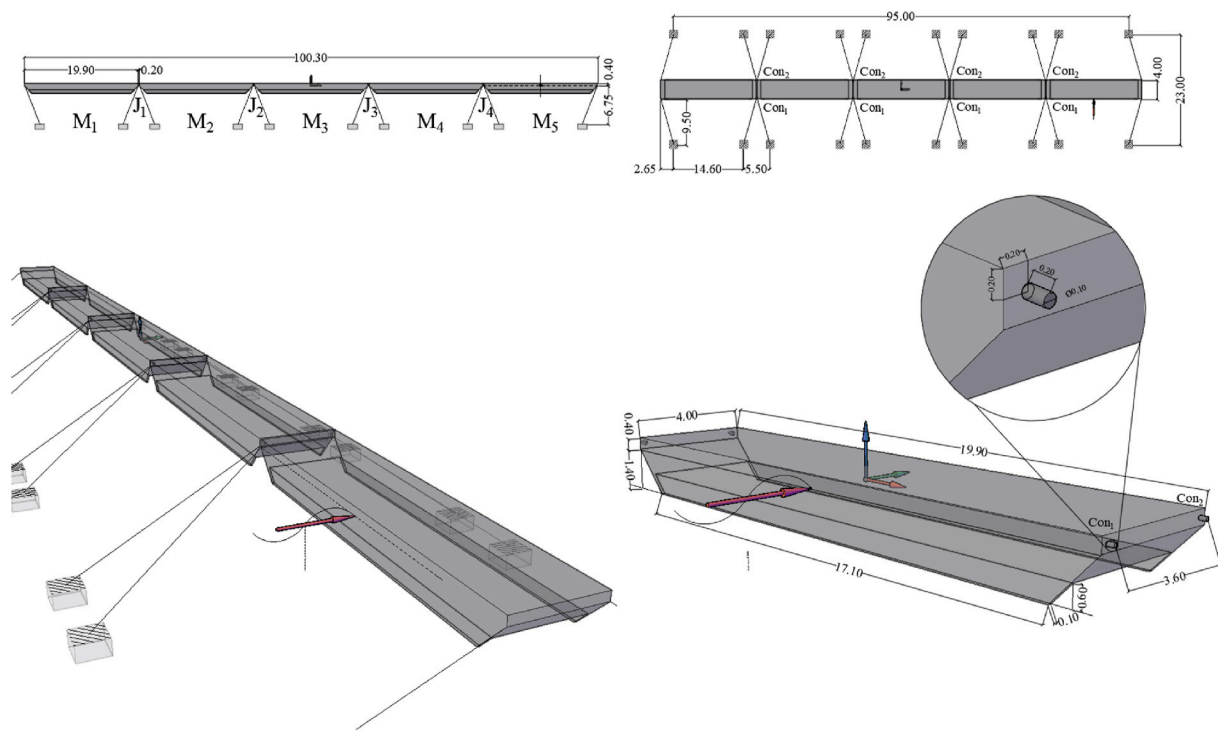


Fig. 3. Main floating breakwater elements and dimensions (in [m]). *M* denotes the module number, *J* is the joint number and *Con* is the connection number. Based on Peña et al. (2011).

Table 1
Geometrical and mechanical properties of the modular pontoon.

| Property | Axis | Value |
|-----------------------------|------|---------|
| Length (m) | X | 19.90 |
| Beam (m) | Y | 4.00 |
| Height (m) | Z | 1.80 |
| Draft (m) | Z | 0.40 |
| Depth (m) | Z | 6.75 |
| Displacement (t) | - | 40.00 |
| Centre of gravity (m) | X | 0 |
| | Y | 0 |
| | Z | -0.21 |
| Centre of buoyancy (m) | X | 0 |
| | Y | 0 |
| | Z | -0.42 |
| Inertia (t·m ²) | X | 60.94 |
| | Y | 1253.82 |
| | Z | 1303.98 |
| Radius of gyration (m) | X | 1.23 |
| | Y | 5.60 |
| | Z | 5.70 |

based on potential flow theory have also been applied. Chen et al. (2012) applied a 2-D model to analyse the transmission coefficient, motion response, and mooring forces of a pontoon-plate floating breakwater under regular waves. Later, the 3D motion response performance of a single moored pontoon and the forces in the mooring system were analysed under regular waves with different wave headings Chen et al., 2017. Nonetheless, there are no time-domain simulations of floating pontoon arrays under more realistic wave conditions in the literature.

This study dealt with 3D numerical modelling in the time domain of a modular pontoon breakwater studied experimentally by Peña et al. (2011). The objective was to accurately estimate the forces in the connectors, a critical element in the design of these structures. The forces in the elastic mooring lines and the module connectors were considered along with the instantaneous Froude-Krylov and hydrostatic forces beneath the incident wave surface to include nonlinear effects. First, the

array was simulated under oblique regular waves to calibrate connector stiffness and possible hydrodynamic drag in the fins. Then and as a novelty, more realistic irregular wave conditions were simulated and the results compared with those under regular waves. For this purpose, a set of random realizations under irregular waves were carried out to obtain statistics on the maximum instantaneous forces in the connections.

The remainder of the paper is structured as follows. Section 2 describes the numerical modelling approach applied, including the pontoon geometry, frequency and time-domain analyses, and calibration of the numerical model. The results are presented and discussed in Section 3. Finally, conclusions are drawn in Section 4.

2. Materials and methods

In this study, we analysed the dynamic response of a pontoon-type modular floating breakwater on waves to estimate the module connector forces, a key point in its structural design. The studied breakwater, previously analysed by Peña et al. (2011), was an array of five floating pontoons interconnected with hinged joints and moored to the seabed with elastic lines at a water depth of $d = 6.75$ m. The detailed geometrical properties of the array are summarized in Fig. 3 and Table 1.

The approach was implemented in Aqwa (ANSYS, 2016), a numerical simulation environment that has been applied successfully to the study of other floating marine structures, such as platform-riser coupling systems (Wang and Liu, 2018) and complex structures such as the Mid Water Arch (Hill et al., 2014), or wave energy converters (López et al., 2017). Moreover, it has already been applied to a floating pontoon module under regular waves (Chen et al., 2017).

2.1. Frequency domain analysis

The floating module response in the frequency domain was characterized using Aqwa Line, a 3D BEM code that applies potential flow theory assuming an ideal fluid, and irrotational flow. The breakwater modules are assumed to be rigid bodies with little oscillation, and in this case, with zero forward speed. Under these assumptions, and a Cartesian

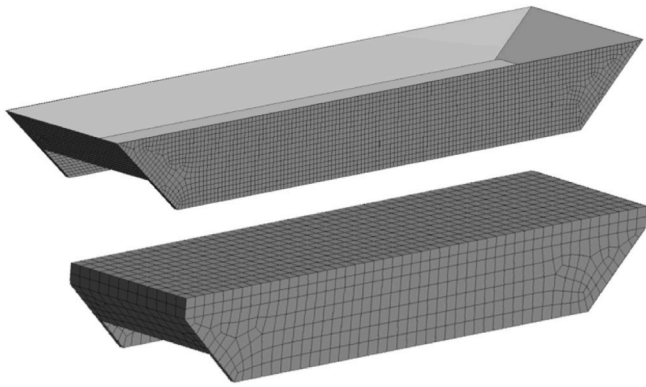


Fig. 4. The individual floating module panel models for the frequency domain analysis (upper panel) and for the time domain analysis (lower panel).

reference system $\mathbf{X} = (X, Y, Z)$, the motion of the fluid around the modules is defined by the velocity potential:

$$\varphi(\mathbf{X}, t) = \text{Re}[\varphi(\mathbf{X})e^{-i\omega t}] \quad (1)$$

where: t is the time, ω is the angular frequency, Re denotes “the real part of” and φ is the velocity potential expressed as a function of the spatial coordinates. This potential is commonly distributed in three different terms: incident potential (φ_i), diffracted potential (φ_d) and potential radiated by the m structure due to its own motion at the j th degree of freedom (DoF). Assuming six DoFs and M interacting structures, these velocity potentials are related as follows:

$$\varphi e^{-i\omega t} = \left[\varphi_i + \varphi_d + \sum_{m=1}^M \sum_{j=1}^6 \varphi_{mj} x_{jm} \right] e^{-i\omega t} \quad (2)$$

where x_j represents the motion of the floating body around the j th DoF. The velocity potential of the fluid was estimated by applying the BEM, which transforms the partial derivative problem formulated into integrable surfaces. The forces in the analysis were applied using the pulsating Green function for finite water depth (Green, 2008), satisfying the following conditions:

- On the free surface ($Z = 0$)

$$-\omega^2 \varphi + g \frac{\partial \varphi}{\partial Z} = 0 \quad (3)$$

where g is the gravitational acceleration.

- The surfaces of the pontoon modules are impermeable, so the velocity of the particles in contact with them is equal to the velocity of the body

$$\frac{\partial \varphi}{\partial n} = \mathbf{u} \cdot \mathbf{n} \quad (4)$$

where $\partial/\partial n$ represents variation in the direction normal to the module surface and \mathbf{n} is the unitary vector normal to the body surface.

- The velocity potential on the seabed ($Z = d$) is equal to zero

$$\frac{\partial \varphi}{\partial Z} = 0 \quad (5)$$

- The radiation condition, where fluid perturbation is dissipated at long distances from the floating module

$$\lim_{R \rightarrow \infty} (\varphi) = 0 \quad (6)$$

for $R = (X^2 + Y^2)^{0.5}$.

For frequency domain analysis of the wave response of a single module in the array, its wetted surface (S_0) was meshed into 12,000 0.35 ± 0.10 -m plane quadrilateral diffracting panels (Fig. 4). A second mesh of 3000 0.50 ± 0.10 -m diffracting panels was used to reduce the computational cost of time-domain simulation of the complete pontoon array, which would require solving the frequency-dependent hydrodynamic coefficients first and then meshing the full geometry (explained in Section 2.2).

Once the potentials had been determined, the dynamics of a free-floating module subjected to wave action was modelled as a mass-spring mechanical system. Motion response in the frequency domain is governed by:

$$[-\omega^2(\mathbf{M} + \mathbf{A}) - i\omega\mathbf{B} + \mathbf{C}] \cdot \boldsymbol{\chi} = \mathbf{f}(\omega) \quad (7)$$

where: \mathbf{M} is the structural matrix; \mathbf{A} is the added mass matrix, which accounts for the effect of acceleration induced by the floating body on the nearest fluid particles; \mathbf{B} is the linear damping matrix, which accounts for the wave radiation phenomenon of oscillating floating bodies; \mathbf{C} is the hydrostatic stiffness matrix; $\boldsymbol{\chi}$ is the motion amplitude of the floating module in each DoF; and $\mathbf{f}(\omega)$ is the vector of unitary forces and moments (frequency dependent) acting on the mean wetted surface (S_0).

Matrices \mathbf{A} and \mathbf{B} are frequency-dependent hydrodynamic coefficients, which depend on the geometry of the body and water depth as given by:

$$\mathbf{A} = \frac{\rho}{\omega} \int_{S_0} \text{Im}[\varphi_r] \mathbf{n} dS, \text{ and} \quad (8)$$

$$\mathbf{B} = -\rho \int_{S_0} \text{Re}[\varphi_r] \mathbf{n}_j dS \quad (9)$$

respectively, where: Im denotes “the imaginary part of”, Re denotes “the real part of”, and ρ is the seawater density. If the pontoon module is considered a floating body with zero forward speed and no current, then \mathbf{A} and \mathbf{B} are symmetric (Faltinsen, 1993). Due to the symmetric geometry of the pontoon around the vertical planes (XZ and YZ) the terms outside the main diagonals (related to these planes) of both matrices are null, so that

$$\mathbf{A} = \begin{pmatrix} A_{11} & 0 & 0 & 0 & A_{15} & 0 \\ 0 & A_{22} & 0 & A_{24} & 0 & 0 \\ 0 & 0 & A_{33} & 0 & 0 & 0 \\ 0 & A_{42} & 0 & A_{44} & 0 & 0 \\ A_{51} & 0 & 0 & 0 & A_{55} & 0 \\ 0 & 0 & 0 & 0 & 0 & A_{66} \end{pmatrix} \quad (10)$$

$$\mathbf{B} = \begin{pmatrix} B_{11} & 0 & 0 & 0 & B_{15} & 0 \\ 0 & B_{22} & 0 & B_{24} & 0 & 0 \\ 0 & 0 & B_{33} & 0 & 0 & 0 \\ 0 & B_{42} & 0 & B_{44} & 0 & 0 \\ B_{51} & 0 & 0 & 0 & B_{55} & 0 \\ 0 & 0 & 0 & 0 & 0 & B_{66} \end{pmatrix} \quad (11)$$

The linear hydrostatic stiffness matrix \mathbf{C} is given by the geometry of the floating pontoon (CoG position and wetted surface) and the density of the fluid. Since the CoG is above the centre of buoyancy (CoB) and both are aligned on the vertical axis, then $\mathbf{C} = \mathbf{C}^T$. Additionally, due to the symmetry of the pontoon with respect to both vertical planes, all \mathbf{C} components are null except for those in the main diagonal associated with vertical motion (Faltinsen, 1993). For a single pontoon this is

$$\mathbf{C} = \begin{pmatrix} 0 & 0 & 0 & 0 & 0 & 0 \\ 0 & 0 & 0 & 0 & 0 & 0 \\ 0 & 0 & 0.80 & 0 & 0 & 0 \\ 0 & 0 & 0 & 0.94 & 0 & 0 \\ 0 & 0 & 0 & 0 & 26.28 & 0 \\ 0 & 0 & 0 & 0 & 0 & 0 \end{pmatrix} \quad (12)$$

with units in $[\text{MN m}^{-1}]$ for $i = j = 1, 2, 3$ or $[\text{MN} \cdot \text{m rad}^{-1}]$, for $i = j = 4, 5, 6$.

The term $\mathbf{f}(\omega)$ in Eq. (7) contains the frequency-dependent unitary force and moment vector applied over the mean wetted surface (S_0). This encompasses the following forces: wave incidence forces, also called Froude-Krylov forces $\mathbf{f}_f(\omega)$, and diffraction forces $\mathbf{f}_d(\omega)$, both considered excitation forces, and radiation forces $\mathbf{f}_r(\omega)$. These forces are estimated based on the velocity potentials as:

$$\mathbf{f}_f(\omega) = -i\omega\rho \int_{S_0} \varphi_f \mathbf{n} dS \quad (13)$$

$$\mathbf{f}_d(\omega) = -i\omega\rho \int_{S_0} \varphi_d \mathbf{n} dS \quad (14)$$

$$\mathbf{f}_r(\omega) = -i\omega\rho \int_{S_0} \varphi_m \mathbf{n}_m dS \quad (15)$$

Once the harmonic response has been solved, the amplitude of the motions in each DoF can be expressed by the Response Amplitude Operator (RAO), which is defined as the response amplitude of the body motion (at each DoF) divided by half the incident wave amplitude (H):

$$\text{RAO}_j = \frac{2\chi_j}{H} \quad (16)$$

The natural oscillation frequencies, or natural modes, which cause resonance vibrations, can be found with the RAOs. The natural periods of a free floating pontoon tend to infinity for DoFs on the horizontal plane (surge, sway and yaw), since no restoring forces are acting on the structure, while the natural modes contained on the vertical plane are expected to be lower, since gravity acts as a restoring force (Faltinsen, 1993).

2.2. Time domain analysis

Time domain simulations were carried out for the complete module array to analyse the forces on the floating pontoon connectors accurately. First, simulations were conducted under regular wave conditions to calibrate the model with the experimental results of Peña et al. (2011). Then, structural performance was analysed under realistic irregular wave conditions, and the results were compared to regular waves.

2.2.1. Numerical modelling description

Aqwa-Naut was used to account for the variation in the instantaneous wetted surface of the floating bodies and then reproduce nonlinear hydrodynamic effects. Therefore, the complete geometry of the modules was meshed, rather than just meshing the mean wetted surface (Fig. 4). The Froude-Krylov and hydrostatic forces over the instantaneous wetted surface of the pontoons were recalculated for each simulation time step along with the forces in the connectors and the mooring lines. The numerical modelling procedure is described below.

\mathbf{x} is the displacement of a floating pontoon from its hydrostatic equilibrium. The numerical approach can be described with the following motion equation:

$$\mathbf{M} \cdot \ddot{\mathbf{x}} = \mathbf{f}_h(t) + \mathbf{f}_f(t) + \mathbf{f}_d(t) + \mathbf{f}_r(t) + \mathbf{f}_c(t) + \mathbf{f}_m(t) + \mathbf{f}_{dr}(t) \quad (17)$$

The total instantaneous force applied over all of the panels consists of hydrostatic forces $\mathbf{f}_h(t)$, Froude-Krylov forces $\mathbf{f}_f(t)$, diffraction $\mathbf{f}_d(t)$, radiation $\mathbf{f}_r(t)$, connection forces between pontoons $\mathbf{f}_c(t)$, mooring forces $\mathbf{f}_m(t)$ and drag $\mathbf{f}_{dr}(t)$.

The nonlinear hydrostatic force $\mathbf{f}_h(t)$ acting on the instantaneous wetted surface, $S(t)$, is calculated as the balance between the gravitational forces $\mathbf{f}_g(t)$ and the upward buoyant forces as:

$$\mathbf{f}_h(t) = \mathbf{f}_g(t) + \rho g \int_{S(t)} p_{st}(t) \mathbf{n} dS \quad (18)$$

where $p_{st}(t) = -\rho g z(t)$ is the instantaneous static pressure.

Incident wave forces $\mathbf{f}_f(t)$ are also dependent on the instantaneous wetted surface and are calculated for each time step as:

$$\mathbf{f}_f(t) = \int_{S_t} p_{dyn}(t) \mathbf{n} dS \quad (19)$$

where $p_{dyn}(t)$ is the dynamic pressure on the body calculated by the Wheeler stretching method (Elchahal et al., 2009).

Diffraction forces include contributions from all the diffracting panels (those contained in the mean wetted surface, S_0), and are found with:

$$\mathbf{f}_d(t) = - \int_{S_0} p_d(t) \mathbf{n} dS \quad (20)$$

where $p_d(t) = i\omega\rho\varphi_d e^{-i\omega t}$ is the diffraction pressure in which the quadratic terms are neglected.

Past motions of the floating body, also called the ‘‘memory effect’’ (Cummins, 1962), are captured by the radiation force term $\mathbf{f}_r(t)$. This is found by the convolution impulse-response function and inertia due to the added mass for an infinite frequency (\mathbf{A}_∞):

$$\mathbf{f}_r(t) = -\mathbf{A}_\infty \ddot{\mathbf{x}}(t) - \int_0^t \mathbf{H}(t-\tau) \cdot \ddot{\mathbf{x}}(\tau) d\tau \quad (21)$$

where \mathbf{H} is the impulse-response function:

$$\mathbf{H}(t) = \frac{2}{\pi} \int_0^\infty \mathbf{B}(\omega) \frac{\sin(\omega t)}{\omega} d\omega = \frac{2}{\pi} \int_0^\infty [\mathbf{A}(\omega) - \mathbf{A}_\infty] \cos(\omega t) d\omega \quad (22)$$

The term $\mathbf{f}_m(t)$ corresponds to the force on the mooring lines. Each mooring line is modelled as a linear-elastic cable. The instantaneous traction force on these elements is estimated as:

$$\mathbf{f}_m(t) = \begin{cases} 0 & \text{if } L(t) \leq L_0 \\ K_m(L(t) - L_0) & \text{if } L(t) > L_0 \end{cases} \quad (23)$$

where: $L(t)$ is the instantaneous cable length, L_0 is the starting cable length, and $K_m = 30 \text{ kN m}$ is the mooring line stiffness. According to Peña (Peña et al., 2011), these mooring lines have a cable pretension of 30%.

The term $\mathbf{f}_c(t)$ includes the 6 DoF forces on the connection elements (Con) (Fig. 3), which are modelled as rigid elements connected to the floating modules through one joint at each end. These joints allow rotations between the floating module and the connection elements but not translations. The restoring moment (\mathbf{M}) in each connection element is given by:

$$\mathbf{M} = - \begin{bmatrix} K_{rx} & 0 & 0 \\ 0 & K_{ry} & 0 \\ 0 & 0 & K_{rz} \end{bmatrix} [0, \mathbf{G}^T] [\mathbf{U}_p - \mathbf{U}_c] \quad (24)$$

where K_{rx} , K_{ry} and K_{rz} are the rotation stiffness around the main axis, \mathbf{G}^T is the unitary change-of-basis matrix from the local axes to the main axes, and \mathbf{U}_p and \mathbf{U}_c are the translation and rotation matrices of the pontoon and connectors, respectively. Given the geometrical disposition of the pontoons and connectors, rotation around X and Z is also restricted and, thus, only the stiffness of the Y axis (K_{ry}) requires calibration.

The time domain simulations explain the nonlinear damping by the pontoon fins modelled using Morison disc elements on the lower half of each fin. The drag forces (\mathbf{f}_{dr}) on these elements are computed as

$$\mathbf{f}_{dr} = \frac{1}{2} \rho D C_d \alpha u_{RMS} (\mathbf{u}_f - \mathbf{u}_s) \quad (25)$$

where D is the disc diameter (set according to fin area); C_d is the characteristic drag coefficient considered one parametric variable for

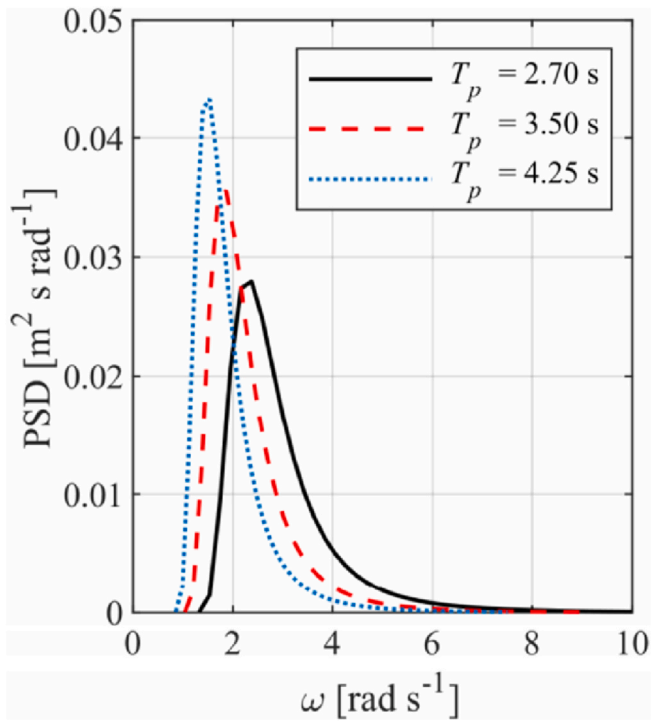


Fig. 5. Examples of the Pierson-Moskowitz power density spectra used for the simulations in the time-domain under irregular wave conditions.

calibration; α is a linearization parameter $\alpha = (8/\pi)^{0.5}$ (Borgman, 1967); u_{RMS} is the root mean square velocity between fluid and structure, and \mathbf{u}_f and \mathbf{u}_s are the relative velocity between fluid and floating structure, respectively.

2.2.2. Numerical model calibration

Drag coefficient C_d and stiffness K_{ry} in the numerical model were unknown and required calibration. The results from the experiments in (Peña et al., 2011) were used to this purpose. The experimental data corresponded to six experiments under regular waves with same wave height of $H = 0.6$ m and wave heading direction of $\theta = 30^\circ$, and six different wave periods of $T = [2.70, 3.10, 3.50, 3.70, 3.85, 4.25]$ s. These cases were reproduced with the numerical model for different combinations of K_{ry} and C_d to calibrate their values. In view of the water depth and wave conditions, the exciting forces on the pontoons were modelled with the second-order Stokes wave theory.

For each simulation, the average amplitude of the moments around the vertical axis, $M_z(t)$, was obtained after the ramping period. Then, the normalized root mean square error (NRMSE) between the amplitudes of $M_z(t)$ obtained numerically and experimentally for the six cases was computed and assigned to the corresponding pair of K_{ry} and C_d values. Accordingly, it was assumed that the lower is the NRMSE, the better is the fit of the simulations to the experiments.

2.2.3. Irregular wave conditions

Once the panel model was calibrated, the behaviour of the floating breakwater under long-crested irregular waves was analysed using the Pierson-Moskowitz spectrum, which presents a power spectral density (PSD) that is often defined as (DNV, 2017):

$$PSD(\omega) = \frac{5}{16} H_s^2 \omega_p^4 \omega^{-5} \exp\left(-\frac{5}{4} \left(\frac{\omega}{\omega_p}\right)^{-4}\right) \quad (26)$$

where H_s is the significant wave height given by

$$H_s = 4\sqrt{m_0} \quad (27)$$

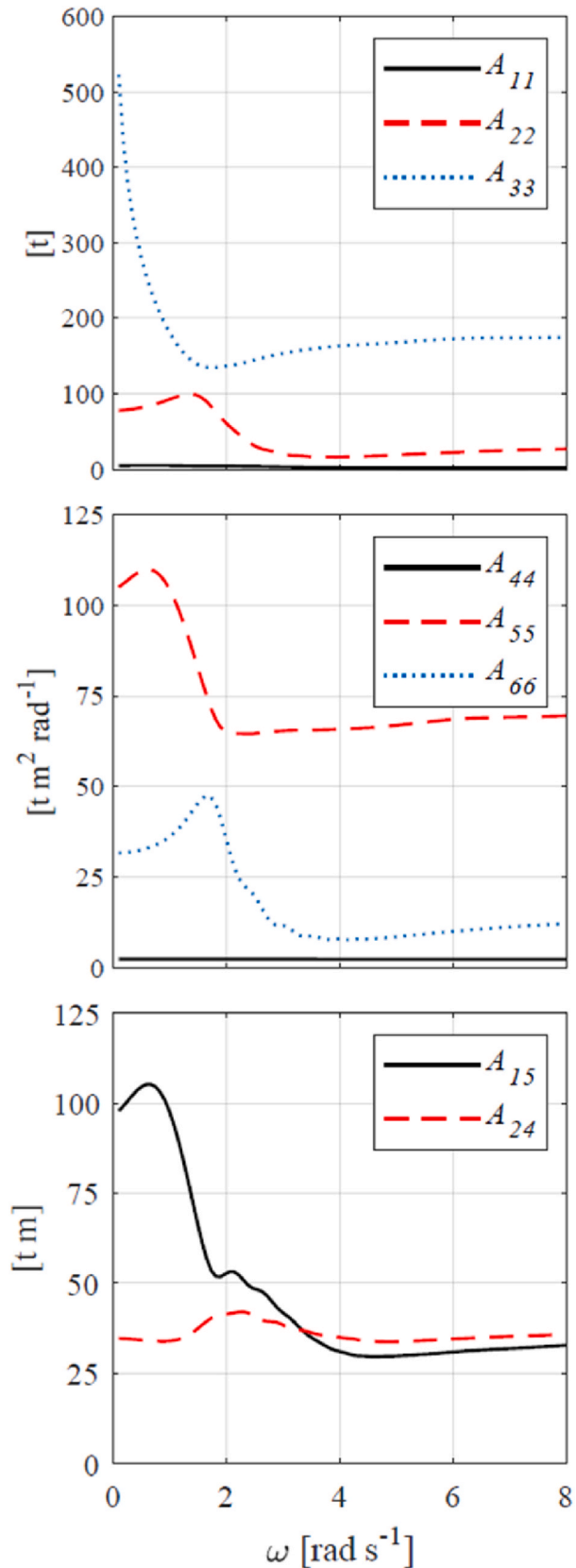


Fig. 6. Components of the added mass matrix (A) of a free-floating module: diagonal elements (upper and intermediate panel) and off-diagonal elements (lower panel).

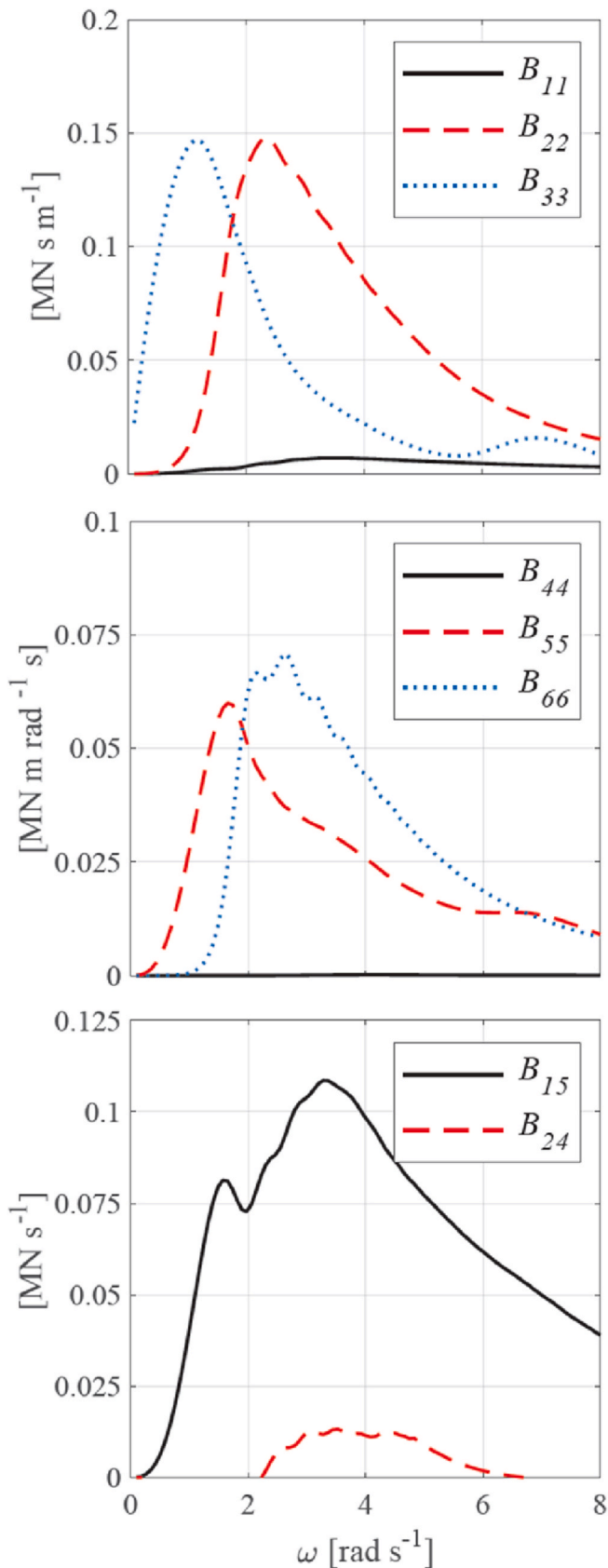


Fig. 7. Components of the hydrodynamic damping matrix (\mathbf{B}) of a free-floating module: diagonal elements (upper and intermediate panel) and off-diagonal elements (lower panel).

with m_0 the zeroth spectral moment (i.e., the area under the spectral curve); and $\omega_p = 2\pi T_p^{-1}$ is the spectral peak frequency, with T_p the peak wave period. More information regarding the derivation of the Pierson-Moskowitz spectrum can be found in (Pierson and Moskowitz, 1964).

Eq. (26) was used to simulate six irregular wave sea states with equivalent wave energy to the six regular wave conditions analysed by Peña et al. (2011). The heading direction for the long crested irregular waves was also maintained from regular waves ($\theta = 30^\circ$). This approach allows comparison between the behaviour of the pontoon array under irregular and regular waves. Regular waves present the same wave energy as an irregular wave spectrum with equivalent root mean square wave height, which is defined as

$$H_{RMS} = \sqrt{8m_0} \quad (28)$$

Considering Eqs. (27) and (28) it results $H_s = (2 \cdot H_{RMS})^{0.5}$. Therefore, a value of $H_{RMS} = H = 0.6$ m was considered for the simulations under irregular waves, which results $H_s = 0.84$ m. As for the peak wave period, equivalent values from the regular wave simulations were used, i.e. $T_p = T = [2.70, 3.10, 3.50, 3.70, 3.85, 4.25]$ s. Fig. 5 shows the Pierson-Moskowitz spectra for several of the sea states simulated.

Additionally, 20 random wave phase spectrums were used to carry out random realizations of each sea state and subsequently calculate statistical parameters relating to the maximums (DNV, 2018). In order to guarantee wave stationarity while minimizing the computational costs, the duration of the simulations was 2000 s. Note that although 3 h is as a standard time between registrations of sea states when measuring waves (Faltinsen, 1993), a sea state can be described as a stationary random process for time periods in the range from 20 min to 3–6 h (DNV, 2017). As for the duration of the time step, it was 0.01 s.

3. Results and discussion

This section discusses the results of numerical simulation of the floating pontoon breakwater. First, the frequency response of a single free-floating module at different wave frequencies and wave heading directions is described. Then, the time response of an array of hinged modules moored to the seabed by elastic lines to regular and irregular oblique waves is presented along with calibration of the numerical model.

3.1. Frequency domain analysis of a free-floating module

3.1.1. Hydrodynamic coefficients

The hydrodynamic coefficients of a single free-floating pontoon were calculated for a combination of 100 angular frequencies (between $\omega_{\min} = 0.10$ and $\omega_{\max} = 8.00$ rad s^{-1}) and 25 wave heading directions (at equal $\Delta\theta = 15^\circ$ intervals). The frequency-dependent coefficients found are described below.

The coefficients in added mass matrix \mathbf{A} are shown in Fig. 6. Among the first three diagonal elements in \mathbf{A} , which relate longitudinal forces to translational accelerations in the same direction, the highest value was for the vertical mode with $A_{33} = 522.80$ t at the lowest frequency. As for the coefficients corresponding to the horizontal translations, A_{22} peaked at $\omega \approx 1.40$ rad s^{-1} with 99.48 t, while A_{11} was below 5.00 t over the entire frequency range. These results are consistent with the geometry of the module, which has a lower cross-sectional area in the longitudinal than in the transverse direction (Fig. 3).

The diagonal elements of \mathbf{A} , which relate moment to rotational acceleration, were highest in pitch mode, where $A_{55} = 110.00$ t m^2 rad $^{-1}$ at $\omega = 0.67$ rad s^{-1} . Vertical rotation peaked at $\omega = 1.70$ rad s^{-1} where $A_{66} = 47.41$ t m^2 rad $^{-1}$, while rotation around the longitudinal axis was negligible ($A_{44} \approx 0$).

Fig. 7 shows the variations in hydrodynamic damping matrix \mathbf{B} with coefficient frequency. The transverse and vertical translational mode values were highest with $B_{22} \approx B_{33} \approx 150$ kN s m^{-1} around $\omega = 2.40$ rad

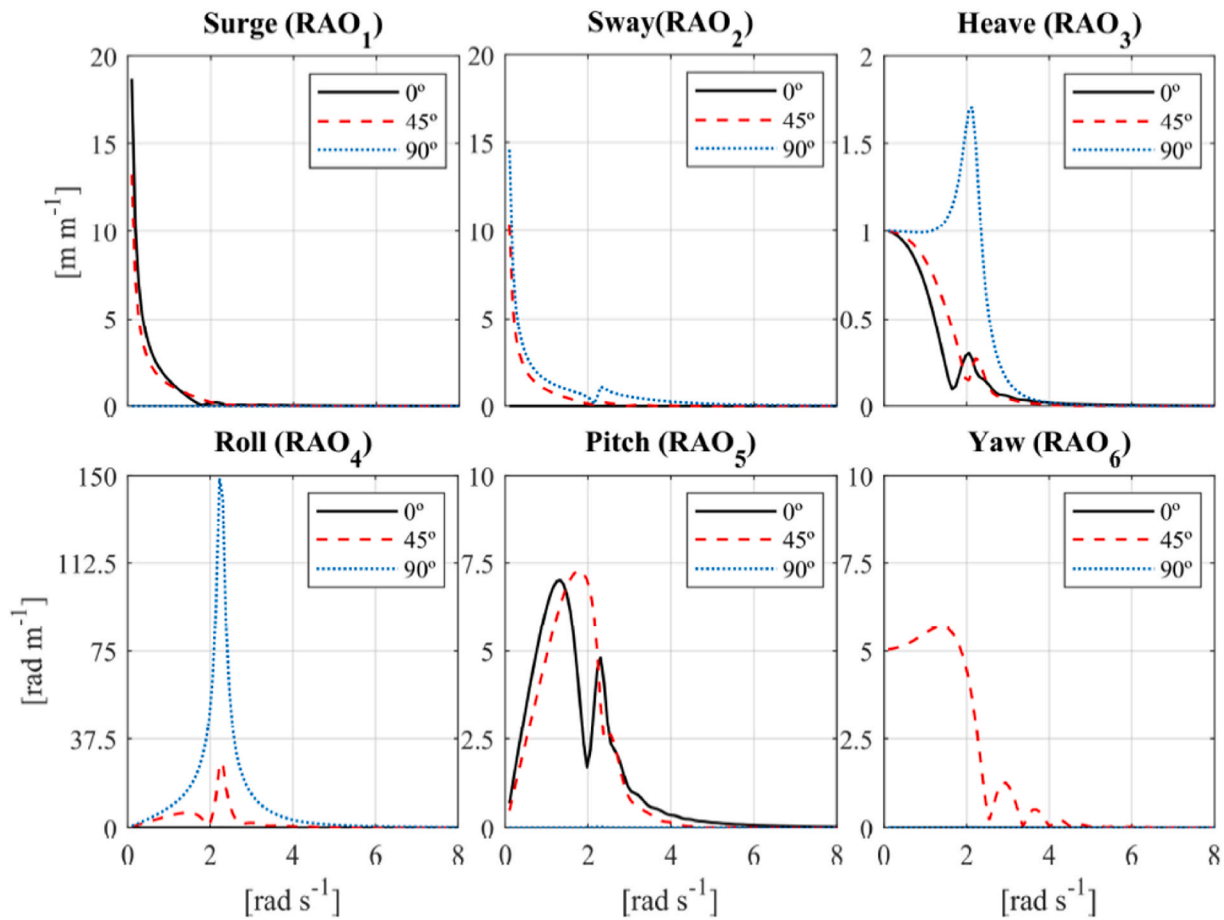


Fig. 8. Response Amplitude Operators (RAOs) without viscous damping effects as a function of the angular frequency (ω) for the 6-DoF and three wave heading directions ($\theta = 0, 45$ and 90°).

s^{-1} and $\omega = 1.20 \text{ rad s}^{-1}$, respectively. The hydrodynamic damping for rotation around these axes peaked at about the same frequencies with $B_{55} = 600 \text{ kN m s rad}^{-1}$ and $B_{66} = 710 \text{ kN m s rad}^{-1}$. In the longitudinal axis modes (B_{11} and B_{44}), damping was rather limited over the full range of frequencies analysed. All coefficients approached zero at low frequencies except for motion-induced damping in heave direction (B_{33}). Coefficients B_{11} , B_{22} , B_{33} and B_{24} also tend to zero at high frequencies within this interval.

As the floating module has zero forward speed and currents are absent, **A** and **B** are symmetric. Furthermore, because the body is symmetrical through both vertical planes, the only nonzero off-diagonal elements in these matrices are those with subindexes 15 and 24. A_{15} peaked at $\omega = 0.60 \text{ rad s}^{-1}$ with 105.20 t m , while A_{24} was lower with a maximum of 41.77 t m . The B_{15} damping coefficient peaked at around $\omega \approx 3.30 \text{ rad s}^{-1}$ with 110 kN m , decreasing to zero at lower frequencies. A similar pattern was found for B_{24} , which peaked at $\omega \approx 3.45 \text{ rad m}^{-1}$ with 10 kN m .

3.1.2. Response Amplitude Operators (RAOs)

Once a hydrodynamic database with the coefficients in **A**, **B** and **C** had been compiled, the modal response of the free-floating module was characterized with Eq. (7). Fig. 8 shows the RAOs for each DoF and three representative wave directions ($\theta = 0, 45$, and 90°). Note that sway, heave, and roll were only activated for normal heading waves ($\theta = 90^\circ$), the same applies to surge, heave and pitch for longitudinal heading waves ($\theta = 0^\circ$).

As expected for a free-floating body, the translational responses on the horizontal plane (surge and sway) increased with the wave period and there were no apparent resonant frequencies. Regarding vertical

translations, a resonant frequency of around $\omega \approx 2.00 \text{ rad s}^{-1}$ was found for the $\theta = 90^\circ$ wave heading, which corresponds to an $\text{RAO}_3 \approx 1.75 \text{ m m}^{-1}$. Apparent peaks at around the same frequency were found for the other two heading directions, but the response was attenuated to less than one in these cases. The response tended toward one at the lowest frequencies (the body oscillates with waves) and tended to zero at the highest.

The highest rotational response was found with roll and a normal heading direction, with a resonant frequency of about $\omega \approx 2.30 \text{ rad s}^{-1}$. Pitch mode showed two resonant frequencies at $\omega \approx 1.30$ and 2.30 rad s^{-1} for the longitudinal wave heading direction, while in the oblique direction, single resonant frequency was around $\omega \approx 1.80 \text{ rad s}^{-1}$.

3.2. Time domain analysis of an array of pontoon modules

3.2.1. Time-domain results under regular waves and numerical model calibration

Once the frequency response of a single module had been characterized, an array of five pontoon modules was simulated in the time-domain under oblique regular waves. The mooring lines and the hinged connections between modules were included in the analysis. The test conditions reproduced were: wave height of $H = 0.6 \text{ m}$, six wave periods of $T = [2.70, 3.10, 3.50, 3.70, 3.85, 4.25] \text{ s}$, and wave heading direction of $\theta = 30^\circ$. The six test cases were simulated for 100 s with a 0.01 s time step in 145 different combinations of C_d and K_{ry} , for a total of 870 simulations. Fig. 9 shows an example of a time series of axial forces, $N(t)$, and yaw moments, $M_z(t)$, for a simulation with $T = 3.5 \text{ s}$, $C_d = 0$ and $K_{ry} = 286.50 \text{ MN rad}^{-1}$.

The error surface found from the 162 NRMSE values is shown in

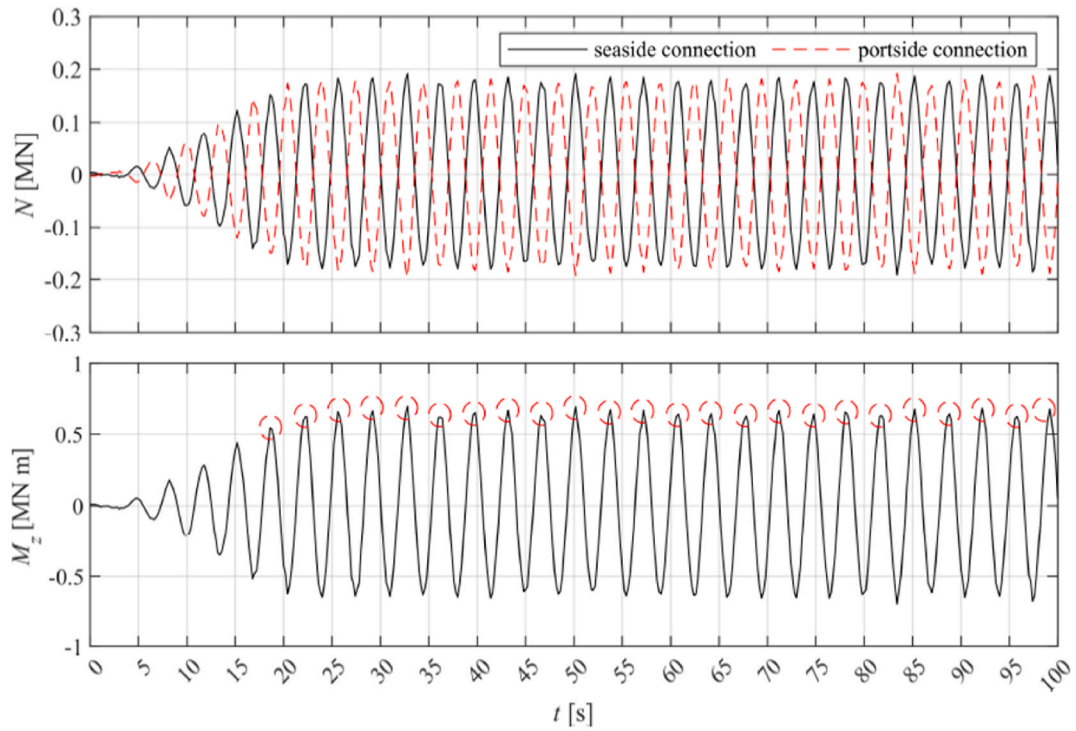


Fig. 9. Time series of axial forces (N) on the connections of joint J_2 (upper panel) and yaw moments on the same joint (M_z) (lower panel). Red circles show the amplitudes after the wave ramp period. Simulation parameters: $H = 0.6$ m, $T = 3.5$ s, $\theta = 30^\circ$, $C_d = 0$ and $K_{ry} = 286.50$ MN rad $^{-1}$. (For interpretation of the references to colour in this figure legend, the reader is referred to the Web version of this article.)

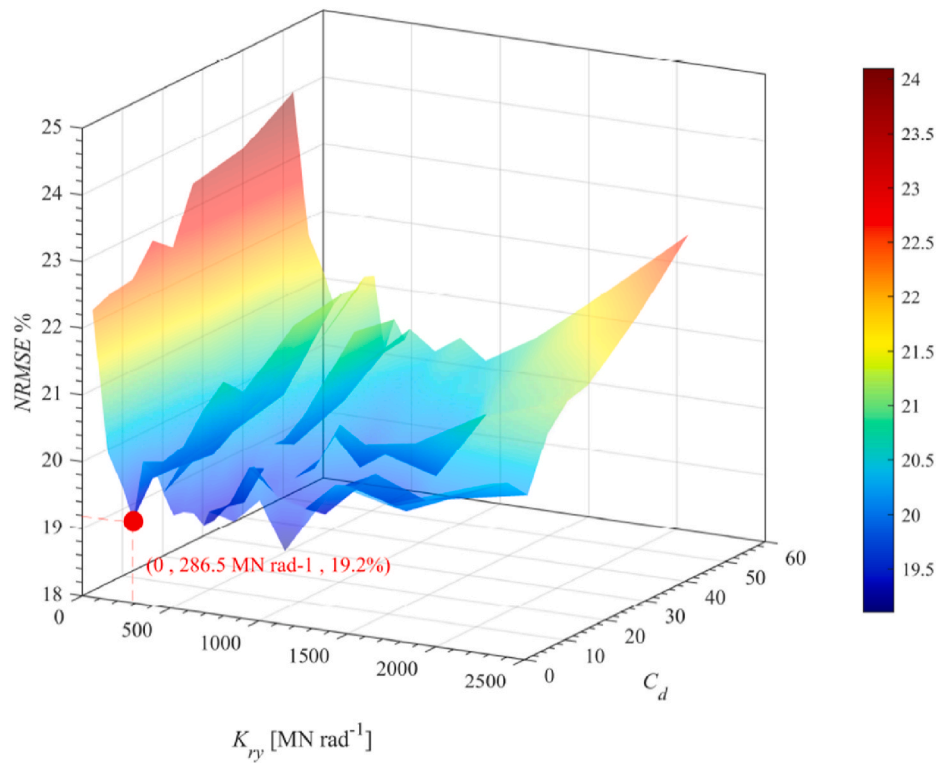


Fig. 10. Normalized Root Mean Square Error (NRMSE in [%]) between M_z obtained for regular wave conditions in the experiments by Peña et al. (2011) and in this work with numerical modelling.

Fig. 10. As observed, the simulation error estimate grew with C_d . In fact, for the same K_{ry} , the error was minimized when C_d tended to zero, which suggests that the hydrodynamic drag of the side fins is negligible. The

results showed a clear pattern in the variation in NRMSE with K_{ry} . The deviation in simulations from the experimental tests increased when this parameter was extreme, reaching an NRMSE over 24%. In other words,

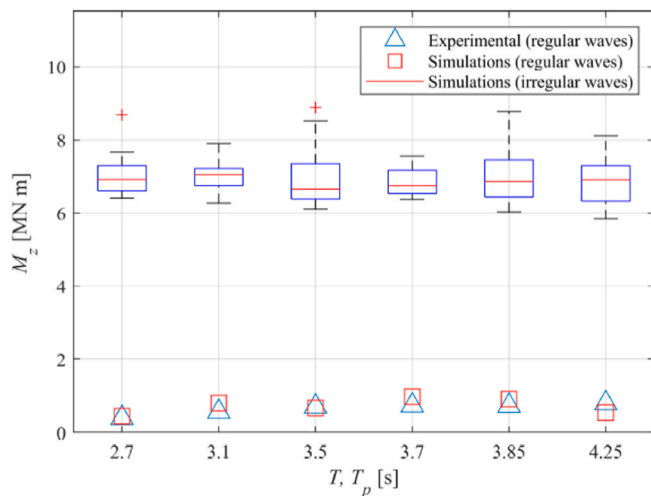


Fig. 11. Maximum M_z for different wave periods found experimentally by Peña et al. (2011) under regular waves, numerically under regular waves and numerically under irregular waves (statistics are provided in boxes: the red central marks indicate the median, the bottom and top edges indicate the 25 and 75th percentiles, the whiskers extend to the most extreme data points not considered outliers, and the outliers are plotted individually using the red '+' marker symbol. Simulation parameters: $C_d = 0$ and $K_{ry} = 286.50 \text{ MN rad}^{-1}$. (For interpretation of the references to colour in this figure legend, the reader is referred to the Web version of this article.)

if the connections in the numerical model are too rigid or too flexible, it is unable to accurately reproduce the force system between the pontoon modules.

$K_{ry} = 286.50 \text{ MN rad}^{-1}$ and $C_d = 0$ minimized the error estimate with an NRMSE = 19%. The M_z found with the numerical model for these values was in good agreement with the results from previous experimental work (Fig. 11). The numerical model is therefore able to reproduce the behaviour of the floating breakwater and, particularly, the forces in the connection system, which is a key issue in its design.

3.2.2. Time-domain results under irregular waves

The time-domain numerical model calibrated in the previous section was used to simulate the behaviour of the same pontoon array, but under more realistic wave conditions. Long-crested irregular waves were reproduced with the Pierson-Moskowitz spectrum (Eq. (26)) preserving the wave energy from the six regular wave conditions in the regular wave analysis. The sea states were for single values of the significant wave height and the wave heading direction ($H_s = 0.84 \text{ m}$ and $\theta = 30^\circ$, respectively), and six different values of the wave peak period ($T_p = [2.70, 3.10, 3.50, 3.70, 3.85, 4.25] \text{ s}$). As an example of the results, Fig. 12 shows samples of the time series of the water surface elevation, $\eta(t)$, the axial forces in the connectors, $N(t)$, and the moments around the vertical axis in a joint, $M_z(t)$, for a particular simulation.

A total of 20 random simulations of each sea state were conducted to obtain their corresponding maximum values of M_z and obtain the statistics for each sea state, which are summarized in Fig. 11. With a unique exception, the maximum moments exceeded $M_z = 6.00 \text{ MN m}$ for all simulations. The highest values were found for the sea state with $T_p = 2.7 \text{ s}$, with an average maximum value of $M_z = 7.71 \pm 0.52 \text{ MN m}$, while the lowest maximums corresponded to the sea state with $T_p = 3.5 \text{ s}$, with an average maximum value of $6.70 \pm 0.58 \text{ MN m}$. The latter values represent a difference in the maximum values of M_z of about 15% between both sea states. In case of regular waves, the differences between the cases with the lowest and highest moments were much lower: if for $T = 2.7 \text{ s}$ the maximum was $M_z = 0.45 \text{ MN m}$, the maximum was $M_z = 0.98 \text{ MN m}$ for $T = 3.7 \text{ s}$, which represents a 118% variation. These results suggest a low influence of the peak wave period in the extreme values of M_z .

On another note, the results for irregular waves showed a significant increase in the maximum moments with respect to the results for regular waves. In fact, the values obtained under irregular waves were one order of magnitude higher than those obtained under regular waves. For instance, the simulation of a regular wave with $T = 3.85 \text{ s}$ resulted in a maximum value of $M_z = 0.91 \text{ MN m}$, while the simulations of an irregular wave sea state of equivalent wave energy and $T_p = 3.85 \text{ s}$ showed average maximum values of $M_z = 6.77 \pm 0.42 \text{ MN m}$ (Fig. 11). These results underscore the importance of including irregular wave conditions in the analysis of the forces and moments of floating pontoon breakwater connections, and discrepancies are wider for regular waves.

4. Conclusions

The performance of a modular pontoon floating breakwater with elastic mooring lines was examined in the time-domain, focusing on the forces and moments on the hinged connections between the modules, which are of paramount importance in their design. The numerical modelling approach applied found the hydrodynamic response of the floating structure in the frequency-domain with a BEM solver first, and then the time-response using the convolution integral method. The instantaneous forces on the structure were recomputed at each simulation step, including the drag forces on the module fins, and the Froude-Krylov and hydrostatic forces on the wetted surface, which reproduced nonlinear effects. The rotational stiffness of the module connections and the drag forces on the fins of the pontoon were calibrated by comparing the results from the simulations with experimental results found previously. Once the model had been calibrated, the response of the array to long-crested irregular waves was compared to monochromatic waves with equivalent energy. Several conclusions of interest can be drawn from the results.

The numerical modelling approach applied can accurately estimate the force system in the connections between the pontoons in a hinged array. In fact, the values of the moments in the joints between modules found with the time-domain numerical model are in good agreement with the results from previous experimental tests in a wave tank.

From the calibration of the numerical model, it may be inferred that the rotational stiffness of the connections strongly influences simulation results. The best fit of numerical to experimental results was given by $K_{ry} = 286.50 \text{ MN rad}^{-1}$ (with NRMSE = 19%). Far from this value, the model was no longer able to accurately reproduce the forces on the pontoon module connections. On the contrary, the drag forces on the fins are negligible, as the drag coefficient that minimized the error between the numerical and experimental results was zero ($C_d = 0$).

With the same wave energy, the maximum moments in the connections were always higher for irregular than for regular waves, with values one order of magnitude higher. These results highlight the need for take irregular wave theory into consideration in future design and verification of these structures.

Summarizing, the force system of an array of pontoons was solved in the time-domain with a BEM numerical model which also applies nonlinear hydrodynamic effects. As a novelty the approach, was applied to model the structure's response not only to oblique regular waves, but also to irregular waves. The calibration with the results from previous experimental work showed a good agreement, which confirms that the methodology is reliable and feasible to estimate the connection forces on these structures. Importantly, it was concluded that irregular wave conditions should be taken into consideration in future studies to avoid underestimating the forces on the connection elements between modules, a key issue in the design of this type of floating breakwater.

CRedit authorship contribution statement

A.J. Cebada-Relea: Conceptualization, Methodology, Software, Formal analysis, Investigation, Resources, Writing – original draft, Writing – review & editing, Visualization. **M. López:** Conceptualization,

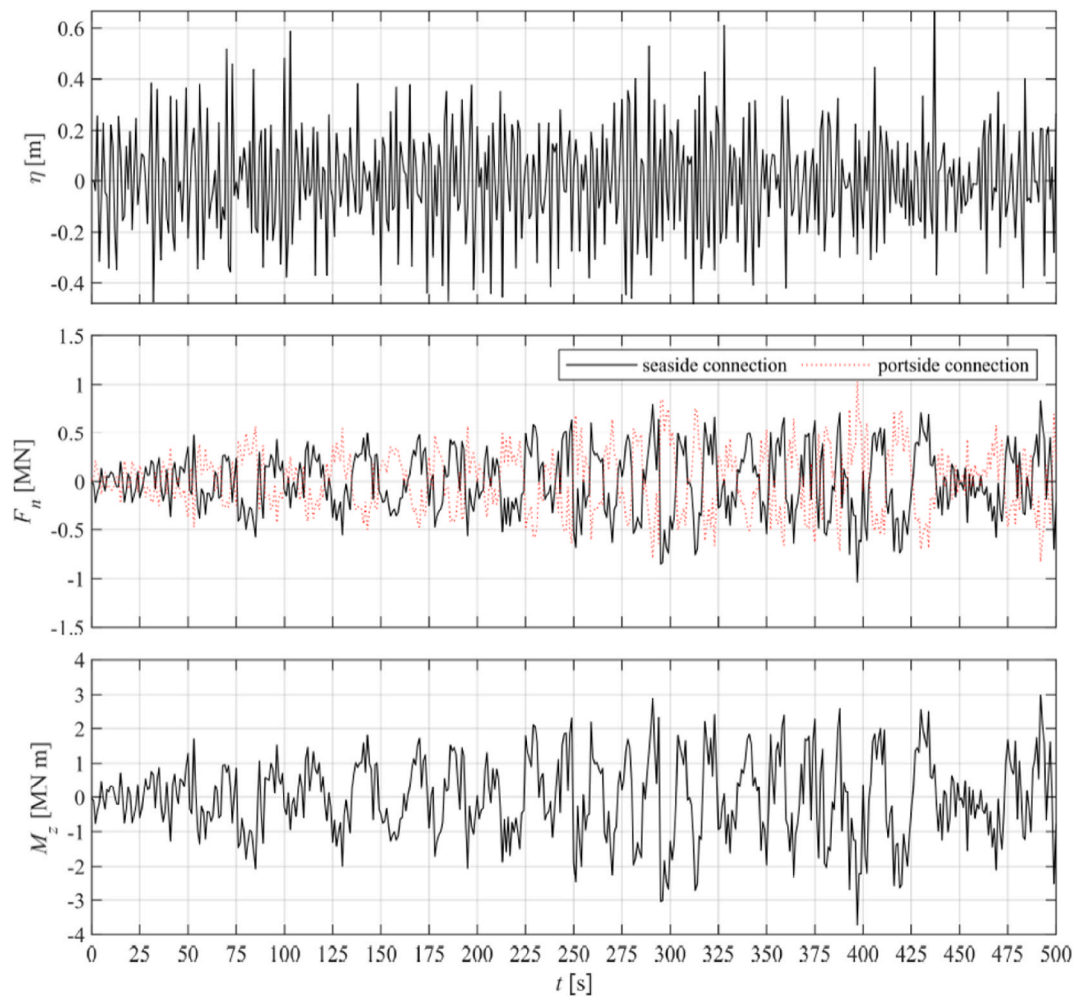


Fig. 12. Time series of water surface elevation (upper panel), axial forces in connections, $N(t)$, in joint J2 (central panel) and yaw moment, M_z , in J2 (lower panel) for an irregular wave with $H_s = 0.84$ m and $T_p = 3.5$ s. As an example and for the sake of clarity, only the first 500 s of the simulation are shown.

Methodology, Software, Formal analysis, Investigation, Resources, Writing – original draft, Writing – review & editing, Visualization, Supervision, Project administration, Funding acquisition. **M. Aenlle:** Conceptualization, Methodology, Investigation, Supervision, Funding acquisition.

Declaration of competing interest

The authors declare that they have no known competing financial interests or personal relationships that could have appeared to influence the work reported in this paper.

Acknowledgments

This research was partially funded by Council of Gijón through the University Institute of Industrial Technology of Asturias, grant number SV-21-GIJON-1-21 (the views and opinions expressed herein do not necessarily reflect those of the University Institute of Industrial Technology of Asturias—IUTA).

A. Cebada received financial aid from the University of Oviedo (Asturias, Spain), under the 2019 Research Aid and Promotion Plan (“Ayudas para realización de Tesis Doctorales. Modalidad A: Contratos de Investigación en régimen de concurrencia competitiva.” [Aid for Ph.D. Dissertation Research, Unit A: Research Contracts with Competitive Funding, Ref. PAPI-19-PF-16]).

Appendix A. Supplementary data

Supplementary data to this article can be found online at <https://doi.org/10.1016/j.oceaneng.2021.110263>.

References

- Abul-Azm, A.G., Gesraha, M.R., 2000. Approximation to the hydrodynamics of floating pontoons under oblique waves. *Ocean Eng.* 27 (4), 365–384.
- Cebada, A., López, M., 2020. Evaluación dinámica para el posible uso de fondeos elástico-lineales en el dique flotante de Figueras (Asturias, España). In: *Proc. 3rd Research, Development and Innovation Conference in Civil Engineering*, pp. 68–71, 2020-October. (In Spanish).
- Borgman, L.E., 1967. Random hydrodynamic forces on objects. *Ann. Math. Stat.* 38 (1), 37–51.
- Ćatipović, I., Ćorak, M., Alujević, N., Parunov, J., 2019. Dynamic analysis of an array of connected floating breakwaters. *J. Mar. Sci. Eng.* 7 (9).
- Chen, Z.J., Wang, Y.X., Dong, H.Y., Zheng, B.X., 2012. Time-domain hydrodynamic analysis of pontoon-plate floating breakwater. *Water Sci. Eng.* 5 (3), 291–303.
- Chen, X., Miao, Y., Tang, X., Liu, J., 2017. Numerical and experimental analysis of a moored pontoon under regular wave in water of finite depth. *Ships Offshore Struct.* 12 (3), 412–423.
- Cheng, L.H., Fen, C.Y., Li, Y.H., Jiang, W.Y., 2020. Experimental study on a new type floating breakwater. *Proc. 7th Int. Conf. Asian Pacific Coasts, APAC 429–433*, 2013, no. Apac.
- Cummins, W.E., 1962. *The Impulse Response Function and Ship Motions*. Department of the Navy, David W. Taylor Model Basin, Hydromechanics Laboratory, Research and Development Report.
- Diamantoulaki, I., Angelides, D.C., 2010. Analysis of performance of hinged floating breakwaters. *Eng. Struct.* 32 (8), 2407–2423.
- Diamantoulaki, I., Angelides, D.C., 2011. Modeling of cable-moored floating breakwaters connected with hinges. *Eng. Struct.* 33 (5), 1536–1552.

- DNV, G.L., 2017. DNVGL-RP-C205: environmental conditions and environmental loads. Recommended Practice. DNV GL.
- DNV, G.L., 2018. DNVGL-CG-0130: Wave Loads. Recommended Practice. DNV GL.
- Dong, G.H., Zheng, Y.N., Li, Y.C., Teng, B., Guan, C.T., Lin, D.F., 2008. Experiments on wave transmission coefficients of floating breakwaters. *Ocean Eng.* 35 (8–9), 931–938.
- Elchahal, G., Lafon, P., Younes, R., 2009. Design optimization of floating breakwaters with an interdisciplinary fluid-solid structural problem. *Can. J. Civ. Eng.* 36 (11), 1732–1743.
- Faltinsen, O., 1993. *Sea Loads on Ships and Offshore Structures*, vol. 1. Cambridge university press.
- Ferreras, J., Peña, E., López, A., López, F., 2014. Structural performance of a floating breakwater for different mooring line typologies. *J. Waterw. Port. Coast. Ocean Eng.* 140 (3), 1–11.
- Green, G., 2008. An essay on the application of mathematical analysis to the theories of electricity and magnetism. *Proc. Camb. Phil. Soc.* 7.
- Hill, J., Laycock, S., Chai, S., Balash, C., Morand, H., 2014. Hydrodynamic loads and response of a Mid water Arch structure. *Ocean Eng.* 83, 76–86.
- Ji, C., Yang, K., Cheng, Y., Yuan, Z., 2018. Numerical and experimental investigation of interactions between free-surface waves and A floating breakwater with cylindrical-dual/rectangular-single pontoon. *China Ocean Eng.* 32 (4), 388–399.
- Lee, J., Cho, W., 2003. Hydrodynamic analysis of wave interactions with a moored floating breakwater using the element-free Galerkin method. *Can. J. Civ. Eng.* 30 (4), 720–733.
- Liu, Z., Wang, Y., 2020. Numerical investigations and optimizations of typical submerged box-type floating breakwaters using SPH. *Ocean Eng.* 209, 107475.
- Lopez, I., Lopez, M., Iglesias, G., 2015. Artificial neural networks applied to port operability assessment. *Ocean Eng.* 109, 298–308.
- López, M., Taveira-Pinto, F., Rosa-Santos, P., 2017. Numerical modelling of the CECO wave energy converter. *Renew. Energy* 113, 202–210.
- Loukogeorgaki, E., Angelides, D.C., 2005. Stiffness of mooring lines and performance of floating breakwater in three dimensions. *Appl. Ocean Res.* 27 (4–5), 187–208.
- Loukogeorgaki, E., Yagci, O., Sedat Kabdasli, M., 2014. 3D Experimental investigation of the structural response and the effectiveness of a moored floating breakwater with flexibly connected modules. *Coast. Eng.* 91, 164–180.
- Loukogeorgaki, E., Vasileiou, M., Rapanta, E., 2015. 3D experimental and numerical investigation of the performance of a modular floating structure. *Proc. Int. Offshore Polar Eng. Conf.* 1548–1555, 2015-Janua.
- Loukogeorgaki, E., Lentsiou, E.N., Aksel, M., Yagci, O., 2017. Experimental investigation of the hydroelastic and the structural response of a moored pontoon-type modular floating breakwater with flexible connectors. *Coast. Eng.* 121, 240–254.
- Martinelli, L., Ruol, P., Zanuttigh, B., 2008. Wave basin experiments on floating breakwaters with different layouts. *Appl. Ocean Res.* 30 (3), 199–207.
- McCartney, B.L., 1985. Floating breakwater design. *J. Waterw. Port. Coast. Ocean Eng.* 111 (2), 304–318.
- Peña, E., Ferreras, J., Sanchez-Tembleque, F., 2011. Experimental study on wave transmission coefficient, mooring lines and module connector forces with different designs of floating breakwaters. *Ocean Eng.* 38 (10), 1150–1160.
- Pierson Jr., W.J., Moskowitz, L., 1964. A proposed spectral form for fully developed wind seas based on the similarity theory of SA Kitaigorodskii. *J. Geophys. Res.* 69 (24), 5181–5190.
- Ruol, P., Martinelli, L., Pezzutto, P., 2013. Formula to predict transmission for π -type floating breakwaters. *J. Waterw. Port. Coast. Ocean Eng.* 139 (1), 1–8.
- ANSYS, 2016. ANSYS Aqwa. ANSYS Ltd., Canonsburg, PA, USA.
- Sannasiraj, S.A., Sundaravadevelu, R., Sundar, V., 2001. Diffraction-radiation of multiple floating structures in directional waves. *Ocean Eng.* 28 (2), 201–234.
- Teng, B., Gou, Y., Wang, G., Cao, G., 2014. And others, “Motion response of hinged multiple floating bodies on local seabed. ” in *the Twenty-Fourth International Ocean and Polar Engineering Conference*.
- Wang, T., Liu, Y., 2018. Dynamic response of platform-riser coupling system with hydro-pneumatic tensioner. *Ocean Eng.* 166 (May), 172–181.
- Williams, A.N., Lee, H.S., Huang, Z., 2000. Floating pontoon breakwaters. *Ocean Eng.* 27 (3), 221–240.